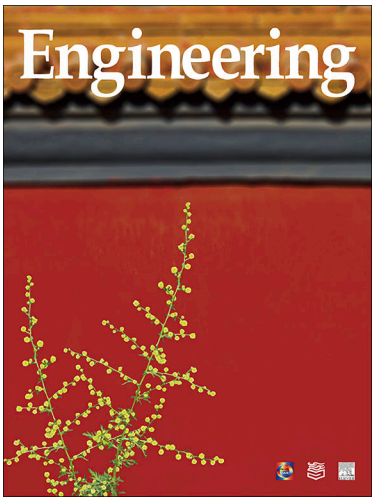
Journal Pre-proofs



Article

Second-Scale Fabrication of Chang'e-6 Agglutinate-Inspired Lunar Glass

Siqi Zhou, Qi Zhou, Feng Li, Wanpeng Li, Baodong Chen, Yutong Deng, Jiayuan Liu, Hao Wang, Yu Jiang, Zhiqian Lin

PII: S2095-8099(26)00573-4
DOI: https://doi.org/10.1016/j.eng.2026.10.006
Reference: ENG 2487

To appear in: *Engineering*

Received Date: 4 September 2025
Revised Date: 14 September 2026
Accepted Date: 13 October 2026

Please cite this article as: S. Zhou, Q. Zhou, F. Li, W. Li, B. Chen, Y. Deng, J. Liu, H. Wang, Y. Jiang, Z. Lin, Second-Scale Fabrication of Chang'e-6 Agglutinate-Inspired Lunar Glass, *Engineering* (2026), doi: https://doi.org/10.1016/j.eng.2026.10.006

This is a PDF of an article that has undergone enhancements after acceptance, such as the addition of a cover page and metadata, and formatting for readability. This version will undergo additional copyediting, typesetting and review before it is published in its final form. As such, this version is no longer the Accepted Manuscript, but it is not yet the definitive Version of Record; we are providing this early version to give early visibility of the article. Please note that Elsevier's sharing policy for the Published Journal Article applies to this version, see: https://www.elsevier.com/about/policies-and-standards/sharing#4-published-journal-article. Please also note that, during the production process, errors may be discovered which could affect the content, and all legal disclaimers that apply to the journal pertain.

© 2026 THE AUTHORS. Published by Elsevier LTD on behalf of Chinese Academy of Engineering and Higher Education Press Limited Company

Research

Civil Engineering Materials—Article

Second-Scale Fabrication of Chang'e-6 Agglutinate-Inspired Lunar Glass

Siqi Zhou [a], Qi Zhou [b], Feng Li [a,*], Wanpeng Li [c], Baodong Chen [c,d], Yutong Deng [a], Jiayuan Liu [a], Hao Wang [a], Yu Jiang [a], Zhiqian Lin [a]

[a] *School of Transportation Science and Engineering, Beihang University, Beijing 100191, China*

[b] *School of Future Aerospace Technology, Beihang University, Beijing 100191, China*

[c] *Beijing Institute of Nanoenergy and Nanosystems, Chinese Academy of Sciences, Beijing 101400, China*

[d] *School of Nanoscience and Technology, University of Chinese Academy of Sciences, Beijing 100049, China*

* Corresponding author.

E-mail address: lifeng98@buaa.edu.cn (F. Li).

ARTICLE INFO

Article history:

Received

Revised

Accepted

Available online

Keywords:

Chang'e-6

In situ resource utilization

Lunar glass fabrication

Ultrafast Joule heating

Lunar soil simulant

ABSTRACT

Journal Pre-proofs

Establishing a sustained human presence on the Moon depends on efficiently converting *in situ* resources into structural materials, thereby reducing the logistical and economic burden of Earth–Moon transport. Agglutinates—complex assemblages of glassy phases, partially melted mineral fragments, and residual crystalline grains formed by micrometeoroid impacts—offer natural templates for high-temperature glass formation. However, the conversion of natural agglutinate structures of lunar soil into engineered glass materials has not been extensively investigated, and conventional furnace-based sintering and hardening techniques for resource utilization typically involve long thermal cycles. In this study, inspired by agglutinates in the Chang'e-6 returned samples, we developed a mineralogically and chemically high-fidelity lunar soil simulant (BH-6) with matched mineral crystal structures, less than 5% deviation in bulk chemical composition, and a median particle size difference of approximately 6 μm. Complete vitrification of compacted BH-6 under vacuum conditions was achieved within approximately 60 s using Joule heating. The resulting glass exhibited a mean relative density of 94.6%, showed no detectable crystalline phases within the detection limit, and exhibited high nanomechanical performance, with hardness exceeding 8.8 GPa and Young's modulus exceeding 106 GPa. Compared to conventional sintering, this method accelerates the glass formation process by two orders of magnitude, offering a new paradigm for rapid lunar glass production and supporting the future development of rapid, on-demand *in situ* resource utilization processing.

1. Introduction

Achieving long-term human presence on the Moon requires the efficient conversion of *in situ* resources into functional materials to reduce the logistical and economic burden of Earth–Moon transportation [1]. As the most abundant material on the lunar surface, lunar soil is a promising resource for *in situ* resource utilization (ISRU) [2–4]. However, converting lunar soil into consolidated engineering materials using conventional furnace-based sintering and hardening techniques typically involves long thermal cycles, including heating, high-temperature holding, and cooling over several hours [5–8]. Even with effective furnace insulation, these processes require a sustained power supply, prolonged temperature regulation, and thermal management, posing challenges for early-stage lunar ISRU systems designed for robotic, on-demand material processing. Therefore, rapid high-temperature processing strategies are needed to shorten processing time while achieving effective densification of lunar-soil-derived materials [9,10].

Agglutinates—complex assemblages of glassy phases, partially melted mineral fragments, and residual crystalline grains formed by micrometeorite impacts—are among the most widespread and structurally complex constituents of lunar soil [11]. The Chang'e-6 (CE6) mission successfully returned approximately 1935.3 g of lunar soil from the Moon's far side [12], with a landing site located in the southern Apollo Basin (41.625°S, 153.978°W) [12,13]. These samples provide valuable far-side lunar regolith constraints relevant to future ISRU studies, although site-specific construction materials near the lunar south pole will require further regional validation. Recent studies [12,14,15] have revealed that CE6 agglutinates primarily comprise quenched glass, partially melted mineral fragments, and residual crystal grains. These components not only record the geological and impact history of the lunar far side [16–18], but also offer a natural structural template and geological precedent for rapid material formation on the Moon [19,20]. Lunar glass is primarily formed by the rapid quenching of large volumes of melt generated by high-velocity meteoroid impacts (15–25 $km \cdot s^{-1}$) [21] or volcanic activity [20]. The glass content in the heavily weathered surface regolith of the Chang'e-5 (CE5) samples generally ranges from 11.6% to 20.0% [22], whereas the amorphous glass fraction in the CE6 samples

is approximately 29.4% [12], reflecting the widespread occurrence of lunar glass throughout lunar geological formation and evolution.

On the Moon, both volcanic activity and meteoroid impacts can generate melts that quench to form glass [23,24]. In particular, micrometeoroid impacts can melt and fuse loose regolith particles into glass-bearing agglutinates. This natural melting–quenching process provides inspiration for transforming lunar soil into consolidated glassy materials through rapid melting and cooling. However, the application of this process to engineered lunar materials remains insufficiently explored, and the mechanisms of rapid densification and material formation remain unclear.

In this study, we establish a second-scale pathway for fabricating mechanically robust lunar glass, guided by the agglutinate structures observed in CE6 samples. By combining die compaction and Joule heating-based rapid sintering, we experimentally validate this strategy on Earth using a lunar soil simulant that closely matches both the composition and structure of the CE6 agglutinates. Although the simulant itself is designed for high fidelity to the lunar regolith, the ultimate goal of the Joule heating process is to transform this loose material into a dense, mechanically robust glass for structural applications. This process substantially reduces the porosity and microdefects inherent in natural agglutinates, surpassing the mechanical performance of the raw soil. In addition, we systematically investigate the glass formation behavior, densification evolution, and their effects on mechanical performance, and compare the results with actual lunar glass. This study provides an experimental basis for rapid glass formation from lunar soil, laying a materials foundation for infrastructure construction in the lunar south polar region.

2. Materials and methods

2.1. Lunar sample preparation and microscopy/microprobe methods

The lunar soil samples used in this study—namely, one CE6 agglutinate clast with a mass of approximately 5.6 mg (sample ID: CE6C0000YJYX068; hereafter, CE6YX068) and a powder sample of 300 mg (sample ID: CE6C0200)—were provided by the China National Space Administration (CNSA). All samples were embedded in epoxy resin and cross-sectioned, followed by stepwise mechanical grinding and fine polishing. Conductive carbon coating was applied to the prepared surfaces for subsequent electron microscopy and mineralogical analysis (Fig. S1 in Appendix A).

Backscattered electron (BSE) images for petrographic analysis of the CE6 agglutinate sample were acquired using a Zeiss Gemini 450 field-emission scanning electron microscope (SEM; Apreo, Thermo Fisher Scientific, USA) equipped with an energy-dispersive X-ray spectroscopy (EDS; XFlash 60, Bruker, USA) at the Institute of Geology and Geophysics, Chinese Academy of Sciences (IGGCAS). The accelerating voltage was 15.0 kV, and the probe current was 2.0 nA.

The chemical compositions of various mineral and glass regions within the agglutinate were examined via electron probe microanalysis (EPMA). The analyses were performed using a JEOL JXA-8230 electron microprobe (JEOL Ltd., Japan) calibrated with certified mineral standards. An accelerating voltage of 15 kV, a beam current of 20 nA, and a spot size of 2–5 μm, adjusted according to the size of the target area (Fig. S2 in Appendix A), were used. The quantitative elemental data obtained for the major mineral and glass phases in the

CE6 agglutinate were used as reference values for subsequent mineral classification based on image recognition methods.

2.2. Semi-supervised learning-based petrographic classification

SEM–EDS is commonly used to assess the modal abundance of basaltic lunar soil samples and to estimate bulk major-element compositions based on elemental maps. However, in lunar agglutinates, the high abundance and compositional variability of glass phases complicate conventional mineral-classification approaches that rely solely on elemental mapping. To address this challenge, we employed a semi-supervised machine learning method using the random-forest-based pixel-classification software Ilastik [25]. Ilastik is well-suited for processing complex mineral textures, variable contrast, and subtle structural features present in BSE images.

Representative regions with known mineral and glass compositions were first identified via EPMA and manually labeled as training data (Fig. S2). Ilastik was then used to automatically extract distinguishing features—including pixel intensity, color gradients, texture patterns, and spatial context—and classify each pixel in the BSE image as either a mineral or glass phase. This method enables rapid, accurate, and consistent quantification of mineral and glass content in lunar agglutinate samples, substantially improving the robustness and efficiency of petrographic characterization compared to traditional manual approaches.

2.3. Crystallographic analysis and high-fidelity lunar soil simulant preparation

Bulk powder X-ray diffraction (XRD) analysis, which requires destructive grinding, was avoided to preserve the physical integrity of the precious lunar agglutinate. Instead, a high-precision microanalytical approach was used. A focused ion beam (FIB; Scios2 DualBeam, Thermo Fisher Scientific) was used to extract electron-transparent lamellae from targeted mineral and glass regions within the lunar agglutinate. The sections were then transferred to a transmission electron microscope (TEM; Thermo Scientific/FEI Tecnai G2 F20 S-TWIN, FEI Company, USA) for crystallographic and compositional analysis. The mineralogy of each region within the FIB foils was first verified via scanning transmission electron microscopy–EDS (STEM–EDS) mapping. Subsequently, selected-area electron diffraction (SAED) patterns were acquired from identified crystalline domains and matched to reference data from the American Mineralogist Crystal Structure Database (AMCSD) to determine phase identity and crystal structure.

Single-phase mineral precursors, either artificially synthesized or naturally occurring, were selected on the basis of the crystallographic information obtained from SAED analysis of CE6 minerals. Diffraction patterns of each raw material were acquired via powder XRD (the diffraction angle 2θ = 10°–90°, Cu Kα radiation), which were then compared with AMCSD reference patterns corresponding to the minerals identified in the CE6 samples. Materials showing good agreement were shortlisted as candidate precursor minerals.

The similarity between the candidate precursor minerals and lunar minerals was further evaluated via laser Raman spectroscopy using a confocal Raman microscope (LabRAM HR Evolution, Horiba, Japan). Raman spectra were acquired using 532 nm laser excitation and focused through a 50× objective lens. The laser power was adjusted to 5.0–7.0 mW depending on mineral type, and Raman signals were collected over 200–1200 cm^{-1}. The instrument was calibrated using the silicon peak at 520.7 cm^{-1}. Each spectrum was acquired with an exposure time of 3–10 s, and eight accumulations were acquired to improve the signal-to-noise ratio.

The chemical compositions of these candidates were subsequently analyzed via X-ray fluorescence spectrometer (XRF; ARLAdvant X IntellipowerTM3600, Thermo Fisher Scientific). A constrained optimization model was developed to closely replicate the major oxide composition of the CE6 samples. The model was used to optimize the mass proportions of seven fundamental mineral components, including clinopyroxene-a, clinopyroxene-b, orthopyroxene, plagioclase, olivine, ilmenite, and quartz. The objective function minimized the sum of squared relative errors for each oxide component. Three constraints were applied: The total mass fraction was constrained to equal 100%, all proportions were constrained to non-negative values, and the deviation of each oxide component from the target value was constrained not to exceed ±5%. The model was numerically solved using the generalized reduced gradient (GRG) nonlinear optimization algorithm [26]. After multiple iterations, an optimal solution satisfying all error constraints was obtained.

A carefully formulated mineral mixture was thermally processed to obtain a synthetic lunar glass that replicated the glassy matrix of the CE6YX068 agglutinate. Based on the recommended phase proportions, plagioclase, clinopyroxene, orthopyroxene, olivine, ilmenite, and quartz were precisely weighed and thoroughly homogenized using a planetary ball mill for 2 h. The resulting powder mixture was then loaded into a custom-designed Joule heating apparatus [27] for melting. The heating setup comprised a horizontally mounted quartz tube serving as a sample holder. A cylindrical sleeve of conductive carbon paper was placed along the inner wall of the tube, forming a closed circuit connected to a power supply. Upon energizing the circuit, Joule heating occurred along the carbon path, generating intense thermal radiation. The mineral mixture, positioned at the center of the quartz tube, was indirectly heated by radiation under high-vacuum conditions (approximately 10^{-3} Pa). The temperature was monitored in real time using a high-precision infrared pyrometer (RJH-2026D, Saiyin New Materials Technology Co., Ltd., China) with a measurement range of 400 to 3600 °C and an accuracy of ±0.5%. The device was calibrated for the specific emissivity of the carbon heating element. The sample was rapidly heated to three target temperatures (1200, 1600, and 1800 °C) and held at each temperature for 60 s. After power shutdown, the molten material underwent rapid quenching under vacuum to prepare simulant lunar glass (Video S1 in Appendix A).

Subsequently, the synthesized glass was milled into a fine powder, which was then mixed with the original mineral powder at a mass ratio of 3:7 and further milled into a fine powder to yield a glass-bearing lunar soil simulant. XRD Rietveld refinement was performed using 10 wt% α-Al_2O_3 as an internal standard to quantify the amorphous glass content in the final simulant. The resulting powder was embedded in epoxy, polished to expose the cross-section, and coated with carbon for imaging. BSE images were acquired, and particle size distributions were quantified using the ImageJ software [28]. These results were compared with the BSE-derived size statistics from the CE6C0200 powder sample; milling and sieving conditions were refined until the difference in median particle size (D_{50}) was less than 10 μm. The final product, designated Beihang-6 (BH-6), exhibited high fidelity in crystallographic structure, chemical composition, and particle size distribution relative to the CE6 lunar soil.

2.4. Lunar glass fabrication and characterization via Joule heating

The BH-6 simulant powder was pressed into pellets measuring 13 mm in diameter under a uniaxial load of 6 tonnes using a hydraulic press to improve the densification of lunar glass. The pellet dimension was selected to match the sample holder and heating zone of our laboratory-scale Joule heating apparatus used for parametric optimization. In this configuration, the specimen was not directly electrically heated; instead, electric current

was passed through the surrounding carbon-based heater, which generated a high-temperature environment and heated the pellet primarily through thermal radiation and conduction. Therefore, the process is not restricted to thin-sheet specimens, provided that the specimen can be uniformly surrounded by the carbon-based heating element [29]. In this study, a 2-cm-thick carbon felt was used as a thermal buffer, and a circular cavity with a diameter of 15 mm and a depth of 3 mm was carved into the carbon felt to hold the pellet during sintering. The throughput may be improved for future small-batch processing by parallel heating of multiple small pellets using multi-cavity or matrix-type sample holders, following the concept demonstrated in related Joule-heating studies [27]. The BH-6 pellets were sintered at 1200, 1400, and 1600 °C for 60 s to obtain glassy products with varying degrees of amorphization.

The sintered products were crushed using a planetary mill and sieved through a 200-mesh sieve (~75 μm aperture). Each sample was mixed with 10 wt% α-Al_2O_3 as an internal standard and analyzed via powder XRD (2θ = 10°–90°, Cu Kα radiation). The amorphous content was quantified via Rietveld refinement. For microstructural evaluation, the sintered pellets were embedded in epoxy resin, polished to expose the cross-sectional surface, and coated with carbon. BSE images were acquired using an SEM, and the evolution of residual crystalline grains, pore morphology, and glass-matrix formation was observed. The SEM observations were used as auxiliary cross-sectional microstructural evidence.

The bulk density of the sintered pellets was determined by the Archimedes method using deionized water as the immersion medium. For each sintering temperature, three independently prepared pellets (n = 3) were measured, and each pellet was weighed three times to obtain an average value. The true density of the corresponding sintered products was measured using a helium gas pycnometer (AccuPyc II 1340, Micromeritics, USA). For true-density measurement, separate portions of the sintered products were fully ground into fine powders using a planetary mill and sieved through a 200-mesh sieve (~75 μm aperture), without adding the α-Al_2O_3 internal standard. The powder samples were dried before measurement to remove adsorbed moisture and to minimize the influence of residual closed pores on the true-density measurements. Each sample was measured five times, and the average value was reported. The relative density was calculated as follows: relative density (%) = bulk density/true density × 100%. The bulk density and true density were reported as mean ± standard deviation (SD), and the uncertainty in the relative density was estimated using standard error propagation from the SDs of the bulk and true-density measurements.

The mechanical properties of the glass were assessed using a nanoindenter (G200X, KLA, USA) with a Berkovich tip at a maximum load of 30 mN. To ensure reproducibility, a constant strain rate of 0.2 s^{-1} was applied during loading, followed by a 1-s hold period at peak load. Thermal drift was corrected by holding at 10% of the maximum load for approximately 80 s during unloading. For the homogeneous sintered BH-6 glass, the nanoindentation tests were performed using a 4 × 4 array of 16 indents with a spacing of 40 μm to obtain statistically representative hardness and Young's modulus values. In contrast, the glass phase in the CE6 agglutinate sample occurred as irregular, micron-scale domains interspersed with vesicles and mineral fragments. Therefore, a targeted indentation strategy was employed: five discrete, defect-free locations within the pure glass phase were carefully selected via optical microscopy to determine the intrinsic mechanical properties, ensuring that the data were not compromised by surrounding impurities or pores.

3. Results and discussion

3.1. Petrographic characteristics of CE6 agglutinates

The CE6 lunar sample exhibits a lithologically complex assemblage, comprising basalts, breccias, agglutinates, glass, and leucocratic fragments [12]. BSE imaging of the selected agglutinate sample CE6YX068, acquired using an SEM, revealed the coexistence of basaltic clasts, brecciated lithic fragments, and diverse glassy phases (Fig. 1(a)–(e) and Figs. S1 and S2), highlighting the mineralogical heterogeneity and microstructural complexity of the lunar agglutinate. This sample serves as a representative object for investigating *in situ* material transformation behavior and provides benchmark compositional and structural data for the preparation of high-fidelity lunar soil simulants. The areal proportions of major components, quantified via EPMA and random forest semi-supervised segmentation using Ilastik [25], were as follows: glass (63.96%), pyroxene (17.7%), plagioclase (14.69%), quartz (1.80%), ilmenite (0.79%), olivine (0.74%), and plagioclase domains with mesostasis (Pl-m, 0.32%) (Tables S1–S6 and Figs. S2 and S3 in Appendix A).

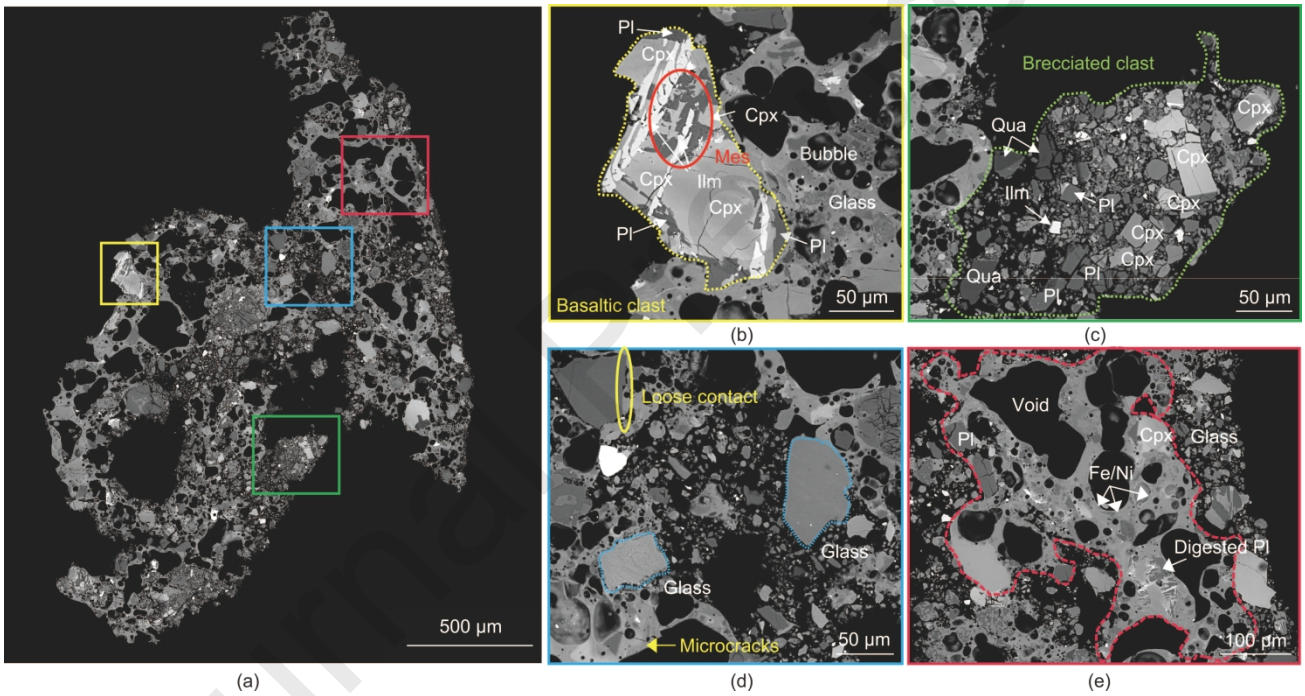


Fig. 1. Microstructural diversity of the CE6YX068 agglutinate. BSE images of the CE6YX068 agglutinate reveal a heterogeneous assemblage of lithic and glassy components. (a) Overview showing the complex microstructure of the agglutinate, with selected areas highlighted. (b) Basaltic clast (yellow) partially enclosed by dense grain-boundary glass, with preserved clinopyroxene (Cpx), plagioclase (Pl), and ilmenite (Ilm), and mesostasis (Mes, red ellipse). (c) Brecciated clast (green) comprising mineral fragments, including clinopyroxene (Cpx), plagioclase (Pl), quartz (Qua), and ilmenite (Ilm), bonded by clast-cementing glass. (d) Homogeneous, inclusion-free glass domain (blue), representing extensive melting and complete mineral digestion. The yellow arrow and circle indicate weak interfaces characterized by microcracks and loose contacts between the glass matrix and mineral phases. (e) Vesicular glass (red) with abundant voids and digested plagioclase fragments, indicating volatile release during rapid quenching.

High-resolution BSE images revealed diverse glass microstructures, indicating multistage and spatially heterogeneous thermal histories. Three major types of glass textures were identified. Grain-boundary glass was observed along clast edges and locally covered mineral surfaces, while the interiors of the mineral grains

remained intact. This texture suggests localized, short-duration heating that caused partial melting (Fig. 1(b)). Clast-cementing glass infiltrated fine-grained breccias and bonded mineral fragments into a coherent matrix, suggesting moderate melting followed by rapid quenching (Fig. 1(c)). Homogeneous, dense glass domains lacking mineral inclusions suggest extensive melting and dissolution of precursor minerals (Fig. 1(d)). Additionally, vesicular textures indicate gas entrapment or release during melting and cooling, while partially digested plagioclase fragments provide further evidence of localized mineral dissolution (Fig. 1(e)).

These diverse morphologies are consistent with the agglutinate formation model proposed for Apollo [30,31] and CE5 soils [19,23,32], wherein fine lunar soil is subjected to instantaneous heating, vaporization, condensation, and rapid cooling during micrometeoroid bombardment. The nonequilibrium structure, porosity, and mineral–glass intergrowths of the glass phase not only reveal the spatial heterogeneity in the formation mechanisms of lunar soil but also provide a natural material template and processing inspiration for the rapid melting and quenching of lunar soil to fabricate mechanically robust glass.

The observed features suggest that high-temperature melting followed by ultrafast quenching is an effective route for producing glass from lunar soil. However, the limited availability and high scientific value of returned lunar samples restrict direct experimental validation. Therefore, high-fidelity lunar soil simulants that replicate the composition and microstructure of natural agglutinates are required to enable ground-based testing of glass formation pathways inspired by real lunar processes.

The CE6YX068 agglutinate comprises key mineral and glass phases—namely, plagioclase, clinopyroxene, orthopyroxene, ilmenite, olivine, quartz, and glass—whose compositions were determined via EPMA (Tables S1–S6). Compared with pyroxenes, plagioclase grains exhibited relatively limited compositional variability, with anorthite content ranging from 84.6 to 97.9. Roughly half of the grains were classified as anorthite ($An_{93.7}Ab_{6.0}Or_{0.3}$), while the others were within the bytownite range ($An_{87.4}Ab_{11.0}Or_{1.6}$) (**Error! Reference source not found.**(a) and Table S1). Here, An, Ab, and Or represent the anorthite, albite, and orthoclase endmembers, respectively. A potassium-rich feldspar with a composition of $An_{67.9}Ab_{4.9}Or_{27.2}$ was also detected in a basaltic clast. Pyroxenes exhibited significant chemical diversity, dominated by augite (average $Wo_{26.2}En_{21.8}Fs_{52.0}$) and pigeonite (average $Wo_{14.6}En_{37.0}Fs_{48.3}$), accompanied by minor orthopyroxene ($Wo_{7.0}En_{68.8}Fs_{24.2}$) (**Error! Reference source not found.**(b) and Table S2). Here, Wo, En, and Fs represent the wollastonite, enstatite, and ferrosilite endmembers, respectively. Olivine grains were predominantly within the Fo_{65} to Fo_{84} range, where Fo denotes the forsterite endmember (Table S4). Average compositions for each major mineral phase were compiled from EPMA datasets and are presented as recommended reference values to support the development of high-fidelity lunar soil simulants (Table S7 in Appendix A). These values serve as stoichiometric targets for the synthetic reproduction of lunar soil analogs.

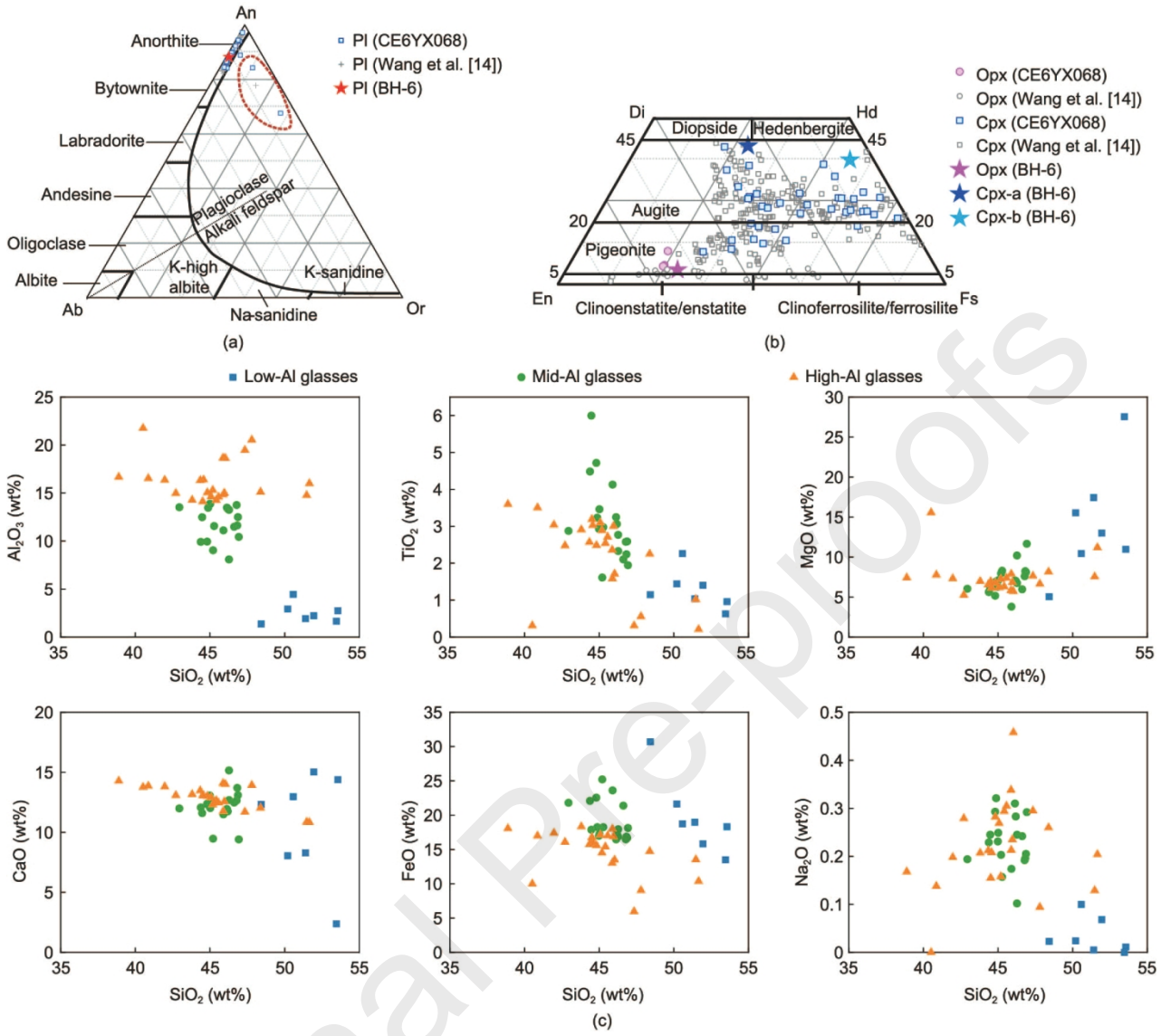


Fig. 2. Major element compositions of minerals and glasses in the CE6YX068 agglutinate compared with literature data and the BH-6 simulant. (a) An–Ab–Or ternary diagram showing plagioclase compositions from CE6YX068 (blue open squares), literature data from Wang et al. [14] (gray crosses), and the BH-6 simulant (red star), demonstrating consistency between natural and synthetic feldspars. (b) En–Fs–Di–Hd ternary diagram showing the compositions of orthopyroxene (Opx; magenta open circles) and clinopyroxene (Cpx; blue open squares) in CE6YX068, compared with literature data from Wang et al. [14] (gray open circles and squares) and BH-6 simulant pyroxenes (blue and cyan stars for Cpx-a and Cpx-b, respectively, and a magenta star for Opx). Cpx-a and Cpx-b denote two clinopyroxene starting materials with distinct chemical compositions, as detailed in Table S7. En, Fs, Di, and Hd denote enstatite, ferrosilite, diopside, and hedenbergite, respectively. The Wo–En–Fs notation used in the main text represents the same pyroxene compositions, with Wo denoting the wollastonite component. The alignment indicates successful replication of lunar mineral chemistry in the BH-6 simulant. (c) Major-element variation diagrams for CE6YX068 glass compositions. Glasses are categorized based on Al_2O_3 content into high-Al (> 15 wt%, orange triangles), mid-Al (5 wt%–15 wt%, green circles), and low-Al (< 5 wt%, blue squares), reflecting compositional diversity derived from plagioclase- and pyroxene-rich lithologies.

The glass phases in CE6YX068 exhibited significant major-element variability (Table S6), reflecting the complex and heterogeneous nature of the precursor materials of the agglutinate. As illustrated in the major

element variation diagrams (**Error! Reference source not found.**(c)), the glasses can be divided into three groups based on the Al_2O_3 content: high-Al (> 15 wt%), mid-Al (5 wt%–15 wt%), and low-Al (< 5 wt%). This compositional spread spans from basaltic (pyroxene-rich) to feldspathic (plagioclase-rich) endmembers, indicating that the glasses likely formed through partial or complete melting and mixing of various lithic clasts during micrometeorite impacts. The broad range of SiO_2 (40.1 wt%–49.9 wt%), Al_2O_3 (2.5 wt%–22.6 wt%), FeO (6.1 wt%–19.8 wt%), MgO (4.1 wt%–14.3 wt%), and CaO (7.1 wt%–18.0 wt%) contents (Table S6) further supports a multi-source origin involving heterogeneous mineral fragments.

Despite this variability, the glass compositions were closely clustered around the bulk composition of CE6YX068 (Table S7), with the maximum deviation in major oxides being only 1.66 wt% for SiO_2 and less than 2 wt% for other components. This compositional convergence indicates that the glasses were formed through extensive melting and effective mixing of mineral fragments, yielding a chemically homogeneous amorphous matrix at the microscale that closely reflects the bulk regolith chemistry.

Such homogenization is consistent with previous observations from Apollo [33–35] and CE5 [19,20,23] samples, where micrometeoroid impacts were shown to induce localized melting, lithic blending, and rapid quenching, generating compositionally variable yet macroscopically representative glass phases. These findings have two key implications. The first is that the glassy component in lunar soil simulants can be reproducibly synthesized by melting high-purity minerals with matching mineralogy and crystallography, ensuring chemical controllability and purity superior to that of natural glasses, where uncontrolled impurities are often present. The second is that the formation of chemically uniform glass within seconds under extreme thermal gradients supports the feasibility of ultrafast *in situ* glass fabrication on the Moon—offering a material strategy compatible with the constrained resources and rapid deployment requirements of lunar infrastructure.

Site-specific cross-sections from representative agglutinate clasts were prepared via FIB milling (Fig. S4 in Appendix A) and subsequently used for structural analysis via TEM. Representative TEM images and the corresponding high-angle annular dark-field STEM–EDS elemental maps from selected FIB foils are shown in Figs. 3(a), (b), (g), (h), (k), and (l). Site-specific regions were selected on the basis of STEM–EDS elemental mapping to enable subsequent phase identification via SAED. Six major crystalline phases were identified, namely plagioclase [36], clinopyroxene [37], orthopyroxene [38], ilmenite [39], olivine [40], and quartz [41]. These phases exhibited sharp diffraction patterns consistent with their known crystal structures (Fig. 3(c)–(e), (i), (j), (m), and (p), and Fig. S5 in Appendix A) and were referenced against the AMCSD patterns (Table S8 in Appendix A). In contrast, glass regions displayed only broad diffuse halos, indicating their amorphous nature (Fig. 3(f) and (n)). Fig. 3(o) shows a bright-field TEM image of an orthopyroxene crystal, while Fig. 3(p) presents the corresponding SAED pattern used for its identification. These findings reveal the complex mineral–glass architecture of the CE6 agglutinate and establish a reliable structural reference for simulant formulation and rapid vitrification pathway development.

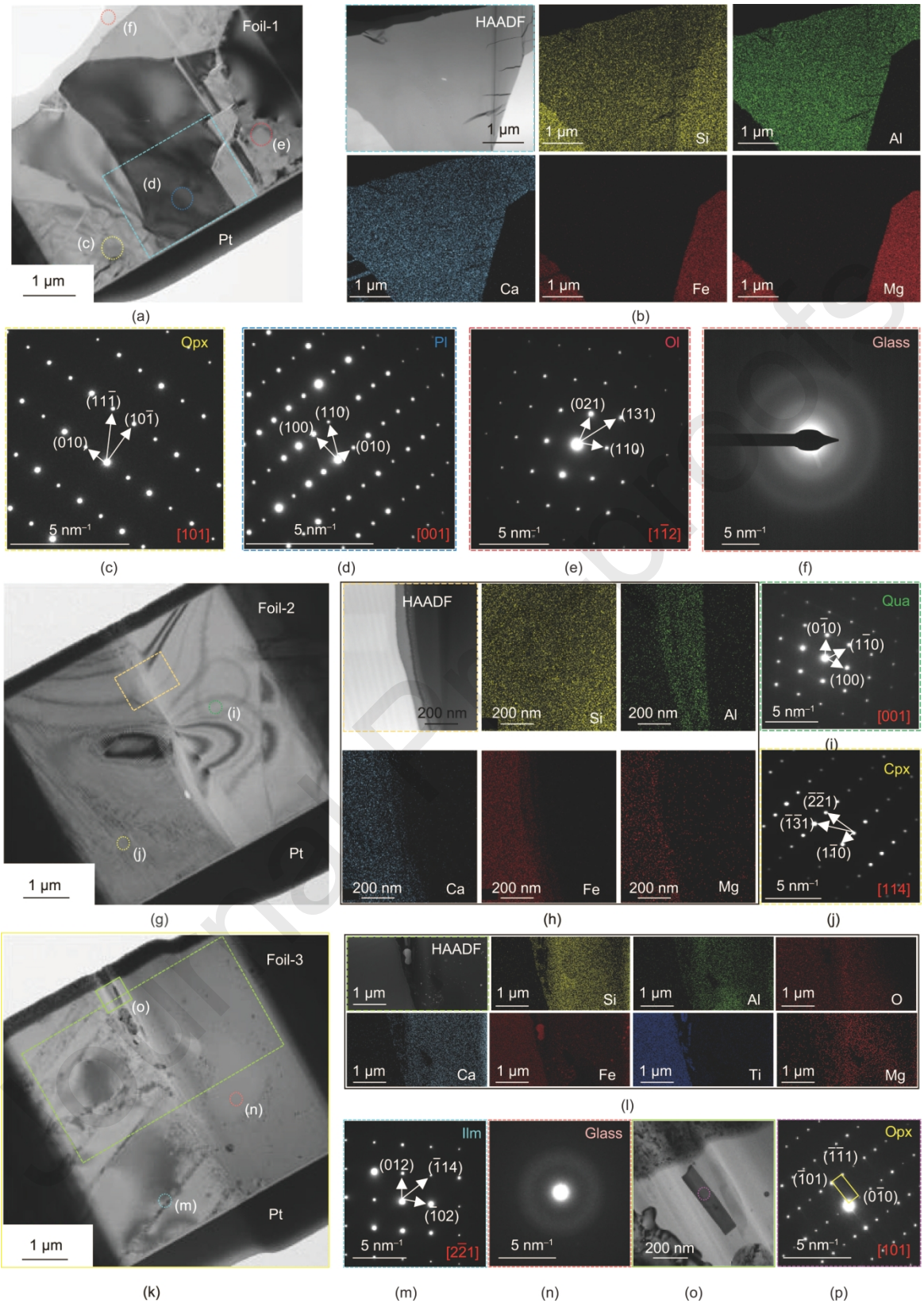


Fig. 3. Structural and crystallographic identification of mineral and glass phases in CE6 agglutinate using TEM, STEM–EDS, and SAED. (a) Bright-field TEM image of Foil-1, with selected regions marked for detailed analysis. (b) Corresponding high-

angle annular dark-field (HAADF) image and elemental maps of Si, Al, Ca, Fe, and Mg acquired via STEM–EDS. (c)–(e) SAED patterns of (c) orthopyroxene (Opx), (d) plagioclase (Pl), and (e) olivine (Ol). (f) Diffuse SAED pattern from an amorphous glass region. (g) Bright-field TEM image of Foil-2, with selected regions marked for detailed analysis. (h) Corresponding HAADF image and STEM–EDS elemental maps. (i) and (j) SAED patterns of (i) quartz (Qua) and (j) clinopyroxene (Cpx). (k) Bright-field TEM image of Foil-3, with selected regions marked for detailed analysis. (l) Corresponding HAADF image and STEM–EDS elemental maps. (m) SAED pattern of ilmenite (Ilm). (n) Diffuse SAED pattern from an amorphous glass region. (o) Local bright-field TEM image showing an orthopyroxene crystal. (p) SAED pattern of the orthopyroxene crystal shown in (o).

3.2. Preparation of high-fidelity lunar soil simulant

Real lunar samples are extremely scarce and of high scientific value. Therefore, we developed a high-fidelity lunar soil simulant, BH-6, based on the mineralogical and glass composition characteristics of CE6 agglutinates, to ensure adequate and stable materials for experimentation. The composition and structure were replicated using a combination of mineral blending and artificial vitrification. High-purity clinopyroxene, orthopyroxene, plagioclase, ilmenite, olivine, and quartz were selected as starting materials. Their XRD patterns closely matched the reference diffraction data of corresponding CE6 minerals in the AMCSD (Fig. 4(a) and Fig. S6 in Appendix A), indicating excellent crystallographic consistency. The XRD pattern of the final BH-6 simulant, incorporating the synthetic glass phase, is shown in Fig. 4 (b). Raman spectra [42] further supported structural similarity (Fig. 4(c) and (d), and Figs. S7 and S8 in Appendix A).

Journal Pre-proofs

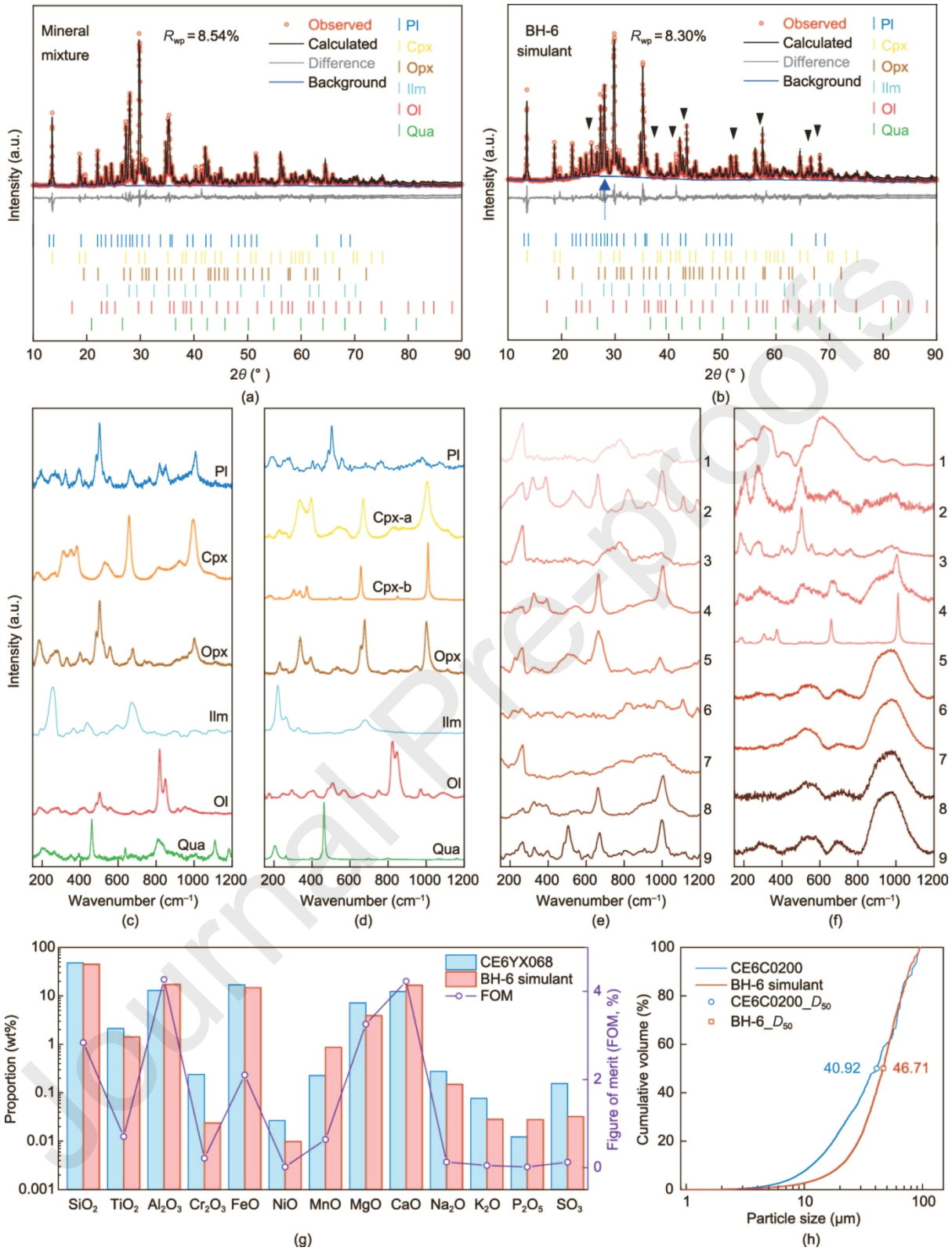


Fig. 4. Characterization of mineral and glass components in the BH-6 lunar soil simulant. (a) XRD Rietveld refinement of the mixed mineral precursors (Section 2 and Table S7). The flat background indicates high crystallinity with negligible amorphous content. A weighted profile *R*-factor (R_{wp}) value of 8.54% confirms the good fitting quality. (b) XRD pattern of the BH-6 simulant, prepared by glass and minerals at a 3:7 mass ratio. 10 wt% α-Al_2O_3 was added as an internal standard

(black triangles) to quantify the amorphous content. A broad hump at 2θ = 20°–40° indicates typical glass features. Rietveld refinement yielded an R_{wp} of 8.30% and an amorphous content of 28.52%, closely matching the expected 30%, validating the effectiveness of Joule heating for full vitrification. (c) and (d) Raman spectra of minerals from (c) the CE6YX068 sample and (d) candidate minerals used in the simulant, showing consistent fingerprint peaks and phase correspondence. (e) Raman spectra of CE6YX068 glass from nine points (Figs. S7 and S8), showing spectral variation. Partially melted zones reveal residual peaks of pyroxene, ilmenite, and quartz, whereas fully amorphous areas show no sharp Raman features. (f) Raman spectra of glasses synthesized at different temperatures: 1–5 (1200 °C), 6 (1600 °C), and 7–9 (1800 °C). Samples heated to 1600 °C or above exhibit complete amorphization, with flattened spectra matching CE6 glass, whereas samples heated to 1200 °C retain mineral peaks. (g) Comparison between the major chemical components of the BH-6 simulant and CE6 agglutinates. The left *y*-axis uses a logarithmic scale to simultaneously visualize both major (e.g., SiO_2) and minor (e.g., K_2O) oxide components, and the specific relative differences are plotted linearly against the right *y*-axis (all within ±5%). (h) Particle size distributions of the BH-6 and CE6C0200 samples. The median particle diameter (D_{50}) difference is below 10 μm, demonstrating good agreement in particle size.

A constrained optimization model was used to optimize the mass ratios of the seven mineral phases to match the overall oxide composition of CE6YX068. The calculated figures of merit [43,44] for all major oxides were maintained within ±5% (2.77%, 4.27%, 4.23%, 3.26%, 2.10%, and 0.77% for SiO_2, Al_2O_3, CaO, MgO, FeO, and TiO_2, respectively) (Fig. 4(g) and Table S7). Although multiple combinations may theoretically satisfy the criterion of < 5% deviation, the GRG algorithm converges to the solution that minimizes the sum of squared errors, representing the mathematical optimum. Furthermore, the solution is physically constrained by the use of the seven specific mineral phases matched to the CE6 sample, ensuring that the recipe is not only chemically accurate but also mineralogically unique and robust.

Unlike conventional simulants that either lack any amorphous phase [8,45,46] or contain compositionally uncontrolled natural glass [47,48], BH-6 incorporates a compositionally tailored artificial glass phase as a key design feature. The glass was prepared via Joule heating at 1800 °C, followed by rapid quenching under vacuum, resulting in an amorphous structure within the detection limit of XRD (Fig. S9 in Appendix A). Its Raman features closely resembled those of the CE6 agglutinate glass (Fig. 4 (e) and (f) and Fig. S10 in Appendix A). Although the analyzed CE6YX068 agglutinate particle exhibited a high localized glass content (approximately 64%) typical of impact-melted aggregates, the bulk lunar soil represents a mixture of these agglutinates with crystalline mineral fragments. The synthesized glass was blended with crystalline minerals at a mass ratio of 3:7 to ensure that the simulant represented the general regolith used for *in situ* construction. This ratio is in good agreement with the average amorphous content (approximately 29.4%) measured in bulk CE6 soil samples by Li et al. [12]. XRD Rietveld refinement revealed a characteristic amorphous hump between 20° and 40°, with good fitting quality, confirming successful glass formation (Fig. 4(b)).

The final BH-6 simulant was obtained through multiple cycles of ball milling and sieving. Its particle size distribution closely matched that of CE6C0200, with median particle diameters (D_{50}) of 46.71 and 40.92 μm, respectively, corresponding to a difference of 5.79 μm (Fig. 4(h) and Fig. S11 in Appendix A). These findings are also in good agreement with the particle size analysis results reported for other powdered CE6 samples [49].

Accurate reproduction of the complex geological evolution of lunar soil—involving long-term space weathering, micrometeoroid bombardment, and solar wind implantation—in a terrestrial laboratory is extremely challenging. Nonetheless, we captured key controlling factors across three scales to realistically replicate lunar soil behavior for *in situ* thermal processing. At the microscale, mineralogical and chemical fidelity is essential because it governs thermodynamic properties such as melting point and melt viscosity. At the mesoscale, the

amorphous-to-crystalline ratio is critical because it determines the rheological flow during sintering. At the macroscale, the particle size distribution determines packing density and thermal conductivity. By strictly matching these parameters, BH-6 ensures valid behavioral extrapolation to real lunar soil, although secondary features such as nanophase iron (np-Fe^0) or specific agglutinate morphologies are not physically replicated.

3.3. Ultrafast fabrication and mechanical performance of lunar soil glass

We conducted Joule heating experiments using BH-6 (Fig. 5(a), upper left) to explore the potential for *in situ* lunar glass fabrication and to address the limitations posed by the scarcity and preciousness of real lunar samples. The BH-6 powder blend was pressed into cylindrical pellets and subjected to Joule heating under vacuum at 1200, 1400, and 1600 °C (Fig. 5(a), upper right, and Fig. S12 in Appendix A). XRD Rietveld refinement and SEM–EDS analysis at different temperatures revealed the vitrification and densification of BH-6.

Journal Pre-proofs

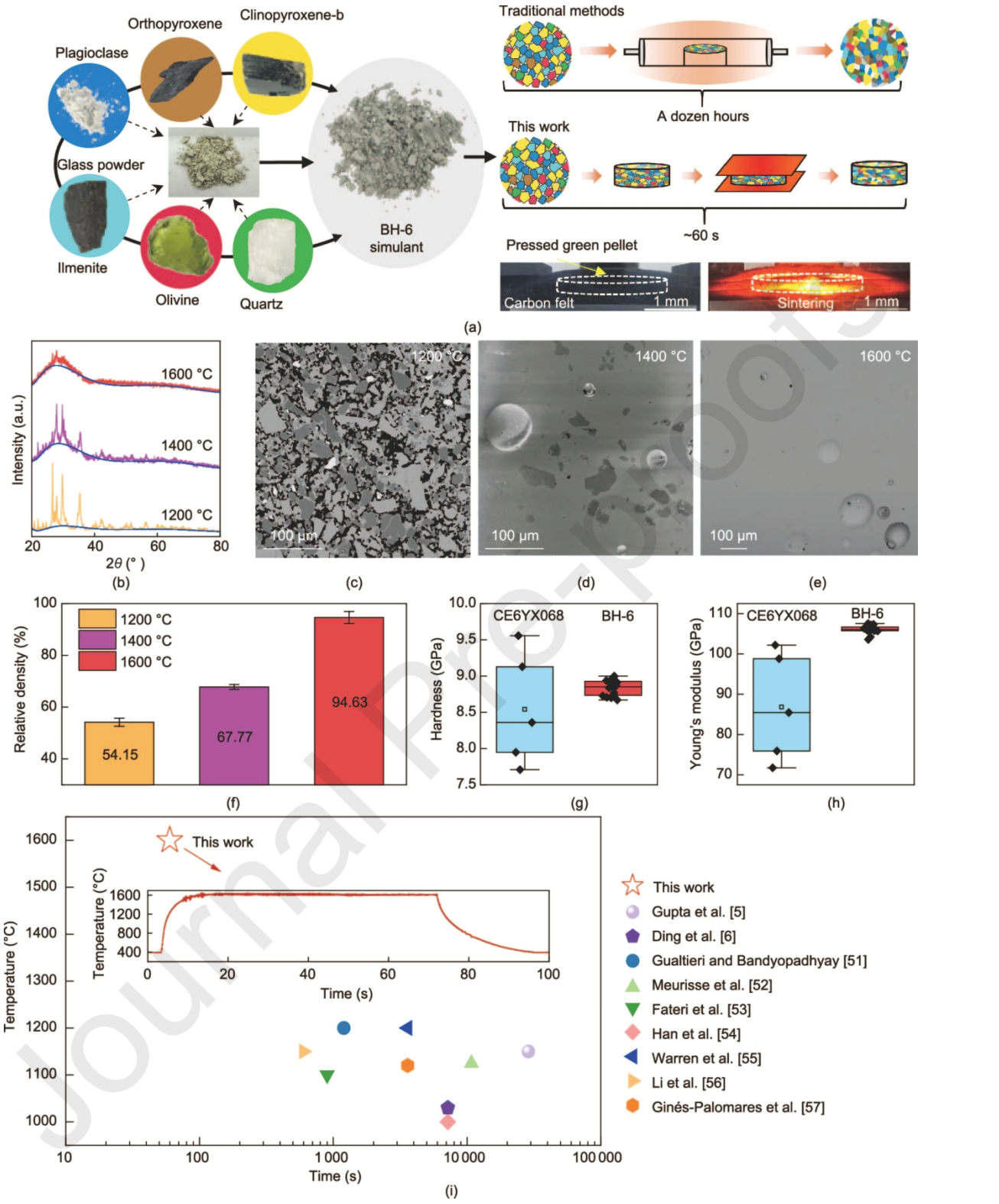


Fig. 5. (a) Raw minerals and the resulting BH-6 simulant, and a schematic of the pellet pressing and Joule heating setup (Fig. S12). (b) XRD patterns of BH-6 samples after Joule heating at 1200, 1400 (Fig. S13 in Appendix A), and 1600 °C for 60 s. (c)–(e) BSE images of sintered samples at (c) 1200, (d) 1400, and (e) 1600 °C for 60 s. (f) Relative density of BH-6 glass samples sintered at different temperatures. (g) and (h) Nanoindentation-derived (g) hardness and (h) Young's modulus of CE6YX068 glass and BH-6 glass sintered at 1600 °C. (i) Temperature profile, sintering schematic, and comparison of the

sintering durations of this study and other reported simulant-based sintering methods [5,6,51–57].

At 1200 °C, the amorphous content of the sintered product reached 50.71 wt% (approximately 20% newly formed glass; Fig. 5(b) and Fig. S13 in Appendix A), accompanied by partial pyroxene melting and grain coalescence. However, unmelted pyroxene, olivine, and plagioclase grains with sharp boundaries were still present (Fig. 5(c)–(e) and Fig. S14 in Appendix A). When the temperature was increased to 1400 °C, a continuous glass matrix was formed, increasing the amorphous content to 76.43 wt% (approximately 46% newly formed). Nonetheless, high-melting-point, Al-rich plagioclase crystals were still observed (Fig. 5(b) and (d), and Figs. S13 and S14). At 1600 °C, original crystalline grains nearly disappeared (Fig. 5(e)), and the XRD pattern exhibited only a broad amorphous hump (Fig. 5(b)). The absence of residual microcrystals at the local scale was further evaluated via micro-area XRD analysis on five randomly selected points using a 50 μm collimator. Consistent diffuse scattering profiles without any Debye diffraction rings (Fig. S15 in Appendix A) were obtained, verifying the largely complete liquid-phase sintering and the formation of a chemically and structurally uniform amorphous solid.

This structural homogenization was accompanied by rapid densification. Bulk-density measurements via the Archimedes method indicated a substantial increase from (1.73 ± 0.05) $g \cdot cm^{-3}$ at 1200 °C to (2.14 ± 0.03) $g \cdot cm^{-3}$ at 1400 °C, reaching (2.84 ± 0.07) $g \cdot cm^{-3}$ at 1600 °C. The true densities of the corresponding sintered products, measured via helium pycnometry, were (3.195 ± 0.003), (3.158 ± 0.006), and (3.001 ± 0.003) $g \cdot cm^{-3}$ for the samples sintered at 1200, 1400, and 1600 °C, respectively. These measured true densities indicate that the relative density increased from 54.15% ± 1.57% at 1200 °C to 67.77% ± 0.96% at 1400 °C and further to 94.63% ± 2.33% at 1600 °C (Fig. 5(f)), suggesting the formation of highly dense lunar glass after second-scale Joule heating. Cross-sectional BSE images from multiple regions provided auxiliary microstructural evidence for the same trend, showing progressive pore isolation and glass–matrix consolidation with increasing temperature (Fig. 5(c)–(e) and Fig. S16 in Appendix A). These results demonstrate that increasing the Joule-heating temperature promoted progressive vitrification, pore isolation, and densification, ultimately producing a lunar glass with a relative density exceeding 94%.

Nanoindentation results showed that the average hardness of the 1600 °C-sintered glass (8.84 GPa) was slightly higher than that of the CE6YX068 glass (8.54 GPa, Fig. 5(g)), and its Young's modulus (106.07 GPa) was significantly higher than that of the CE6YX068 glass (86.82 GPa, Fig. 5(h)). For comparison, a previous nanoindentation study on CE5 lunar glassy particles reported a reduced Young's modulus of 81.7 GPa and a hardness of 7.7 GPa for a hyperaged lunar glass particle [21]. Although the reported modulus is a reduced Young's modulus and the glass composition and aging history differ from those of BH-6, this comparison indicates that the mechanical properties of the 1600 °C-sintered BH-6 glass are within the upper range of the values reported for lunar glass.

This improvement is attributed to the formation of a highly homogeneous amorphous structure during sintering. In contrast, the natural agglutinate contains weak interfaces and intragranular microcracks (Fig. S2), which likely originate from the cumulative effects of long-term micrometeoroid bombardment and thermal cycling on the lunar surface. These structural defects act as compliance sources, significantly reducing the effective stiffness of the material and accounting for the lower Young's modulus of the CE6 glass. Conversely, the Joule-heated BH-6 glass is fabricated under controlled static pressure with a single thermal cycle, yielding a dense and homogeneous glass matrix (Fig. 5(e)) that contributes to improved mechanical performance. The

1600 °C-sintered glass also exhibited narrower distributions in the nanomechanical measurement results: The standard deviations of hardness and modulus were lower by 85.9% and 92.4%, respectively, compared to those of CE6YX068, indicating more uniform and stable properties and suggesting improved microscale mechanical uniformity; nonetheless, macroscale reliability must be further validated (Fig. 5(g) and (h) and Fig. S17 in Appendix A). This improvement is attributed to the full vitrification and elimination of residual crystalline phases. Local mechanical heterogeneity due to residual crystalline phases has been previously observed in CE5 lunar breccia clasts: distinct lithologies display pronounced variations in hardness and modulus at the microscale [50].

Although inspired by the rapid formation of natural lunar agglutinates, our method employs controlled Joule heating to promote more uniform melting and densification. Natural impacts involve transient shock waves and extreme cooling rates, often trapping volatiles to form porous, heterogeneous structures (Fig. 1(e)). In contrast, the Joule heating method utilizes radiative heating under static vacuum. This controlled process substantially reduces pore connectivity and largely digests residual mineral phases, yielding a glass that is structurally denser and mechanically more homogeneous than its natural counterparts.

The Joule heating method demonstrated remarkable time efficiency. Unlike conventional furnace sintering, which typically requires several hours of continuous heating, Joule heating achieved vitrification within 60 s, reducing processing time by nearly two orders of magnitude (Fig. 5(i)) [5,6,51–57]. Conventional sintering is highly effective for mass production on Earth owing to its large batch capacity. However, power availability, thermal management, and operational flexibility under extreme environments must be considered to evaluate the practicality of lunar ISRU processing. To quantify the laboratory-scale energy requirement, we calculated the real-time power and cumulative energy consumption from the measured voltage and current profiles (Fig. S18 in Appendix A). Although the process required a high instantaneous peak power of approximately 0.9 kW at 1600 °C, the extremely short processing duration resulted in a total energy consumption of merely 46.22 kJ for the 13 mm pellet. This indicates a low total energy demand for single-pellet processing. Thus, future lunar implementation will require pulsed operation, temporary energy storage, or power-buffering strategies to accommodate the peak power demand. In some permanently shadowed lunar polar regions, where temperatures can approach approximately 40 K, this second-scale capability is advantageous for on-demand *in situ* hardening because it greatly shortens the duration of high-temperature operation and reduces the requirements for sustained power supply, temperature regulation, and thermal management, particularly when operational agility is prioritized over batch throughput.

Despite these promising results, several limitations remain. First, the experiments were conducted using small laboratory-scale pellets, and the scalability of the Joule heating process requires further investigation. Second, although BH-6 closely reproduces the key compositional and mineralogical characteristics of lunar soil, it does not fully replicate the complex effects of lunar space weathering. Finally, the mechanical performance was primarily evaluated through nanoindentation, and further investigations of macroscale mechanical properties and durability under lunar environmental conditions are needed to assess the feasibility of practical applications.

4. Conclusions

Inspired by the natural formation of glassy agglutinates in CE6 lunar samples, in this study, a second-scale

pathway for fabricating mechanically robust glass from lunar soil was demonstrated. We established a reliable and accessible proxy for systematic experimental investigation by developing the BH-6 simulant—a material exhibiting high fidelity in terms of mineralogy, major oxide chemistry, and particle size distribution relative to its lunar counterpart.

Our results validate that the combination of die compaction and rapid Joule heating can transform the lunar soil simulant into a dense, amorphous, and mechanically robust glass in approximately 60 s. This fabrication time is two orders of magnitude shorter than that required for fabrication via conventional sintering techniques, representing a substantial improvement in processing speed and time efficiency. The resulting glass shows a more homogeneous microstructure than the examined natural agglutinate glass. This, in turn, leads to enhanced and more uniform mechanical properties at the microscale, with a hardness of 8.84 GPa and a Young's modulus of 106.07 GPa.

Despite these promising results, the experiments were limited to small laboratory-scale specimens using simulated lunar soil. Further investigations are needed to evaluate process scalability, energy requirements, macroscale mechanical performance, and long-term durability under lunar conditions. Nevertheless, this study establishes an experimental foundation for rapid, on-demand vitrification of lunar-soil-derived materials and highlights its potential for future lunar ISRU and infrastructure applications.

Acknowledgments

The authors sincerely thank the China National Space Administration for providing the invaluable Chang'e-6 samples (CE6C0000YJYX068 and CE6C0200). We thank Jinhua Li and Lixin Gu at the Electron Microscopy Laboratory, Institute of Geology and Geophysics, Chinese Academy of Sciences (EML, IGGCAS) for their assistance with SEM experiments and mineral-distribution analysis. This study was supported by the National Natural Science Foundation of China (52578496 and 52308427), the Young Elite Scientist Sponsorship Program by the China Association for Science and Technology (YESS20230576), and the Fundamental Research Funds for Central Universities.

Data and materials availability

All data required to evaluate the conclusions reported in the paper are present in the paper and/or the Supplementary Materials.

References

[1] He H, Li L, Hu S, Gao Y, Gao L, Zhou Z, et al. Water abundance in the lunar farside mantle. Nature 2025;643(8071):366–70.

[2] He H, Ji J, Zhang Y, Hu S, Lin Y, Hui H, et al. A solar wind-derived water reservoir on the moon hosted by impact glass beads. Nat Geosci 2023;16(4):294–300.

[3] Zeng X, Wu Y, Yu W, Mo B, Wen Y, Zhao X, et al. Unusual Ti minerals on the moon produced by space weathering. Nat Astron 2024;8(6):732–8.

[4] Yao Y, Wang L, Zhu X, Tu W, Zhou Y, Liu R, et al. Extraterrestrial photosynthesis by Chang'e-5 lunar soil. Joule 2022;6(5):1008–14.

[5] Gupta N, Dawara V, Kumar A, Viswanathan K. Synthetic space bricks from lunar and martian regolith via sintering. Adv Space Res 2024;74(8):3902–15.

[6] Ding M, Chen X, Li Y, Song L, Shi Y, Luo L, et al. Vacuum sintering of the self-developed Chang'e-5 lunar regolith simulant. Constr Build Mater 2024;438:137343.

[7] Jiang Y, Li F, Zhou S, Liu L. Investigating the microscopic, mechanical, and thermal properties of vacuum-sintered BH-1 lunar regolith simulant for lunar *in-situ* construction. Case Stud Constr Mater 2025;22:e04132.

[8] Zhou S, Lin Z, Tao X, Li W, Chen B, Li F, et al. Sintering of Chang'e-5 high-fidelity lunar soil simulant for providing high-strength materials for lunar base construction. Sci China Technol Sci 2025;68(8):1820602.

[9] Zhang X, Liu Y, Zhao S, Song J, Yao W, Wang W, et al. Melting and rapid solidification of lunar regolith particles returned by Chang'e-5 mission. Research 2024;7:0486.

[10] Jiang Y, Zhou Q, Feng Q, Li F, Zhou S. From lunar regolith samples to infrastructure: insights into *in-situ* construction technologies on the Moon. J Build Eng 2025;114:114371.

[11] Li L, Zhang G, Zhang H, Xiao Y, Zhao S, Song J, et al. Transport of volatiles in agglutinates from lunar regolith of Chang'e-5 mission. Research 2025;8:0638.

[12] Li C, Hu H, Yang MF, Liu J, Zhou Q, Ren X, et al. Nature of the lunar far-side samples returned by the Chang'e-6 mission. Natl Sci Rev 2024;11(11):nwae328.

[13] Zeng X, Liu D, Chen Y, Zhou Q, Ren X, Zhang Z, et al. Landing site of the Chang'e-6 lunar farside sample return mission from the Apollo Basin. Nat Astron 2023;7(10):1188–97.

[14] Wang Z, Li Y, Li J, Zong K, She Z, He Q, et al. Chemical compositions of Chang'e-6 lunar soil and substantial addition of noritic crust ejecta from Apollo Basin. Geology 2025;53(7):557–61.

[15] Zhang M, Fa W, Jia B. Provenance and evolution of lunar regolith at the Chang'e-6 sampling site. Nat Astron 2025;9(6):813–23.

[16] Che X, Long T, Nemchin A, Xie S, Qiao L, Li Z, et al. Isotopic and compositional constraints on the source of basalt collected from the lunar farside. Science 2025;387(6740):1306–10.

[17] Zhang QWL, Yang MH, Li QL, Liu Y, Yue ZY, Zhou Q, et al. Lunar farside volcanism 2.8 billion years ago from Chang'e-6 basalts. Nature 2025;643(8071):356–60.

[18] Zhou Q, Yang W, Chu Z, Zhu H, Yang S, Zeng X, et al. Ultra-depleted mantle source of basalts from the South Pole-Aitken Basin. Nature 2025;643(8071):371–5.

[19] Long T, Qian Y, Norman MD, Miljkovic K, Crow C, Head JW, et al. Constraining the formation and transport of lunar impact glasses using the ages and chemical compositions of Chang'e-5 glass beads. Sci Adv 2022;8(39):eabq2542.

[20] Wang BW, Zhang QWL, Chen Y, Zhao W, Liu Y, Tang GQ, et al. Returned samples indicate volcanism on the Moon 120 million years ago. Science 2024;385(6713):1077–80.

[21] Chen Z, Zhao Y, Chi X, Yan Y, Shen J, Zou M, et al. Geological timescales' aging effects of lunar glasses. Sci Adv 2023;9(45):eadi6086.

[22] Li C, Hu H, Yang MF, Pei ZY, Zhou Q, Ren X, et al. Characteristics of the lunar samples returned by the Chang'e-5 mission. Natl Sci Rev 2021;9(2):nwab188.

[23] Zhao R, Shen L, Xiao D, Chang C, Huang Y, Yu J, et al. Diverse glasses revealed from Chang'e-5 lunar regolith. Natl Sci Rev 2023;10(12):nwad079.

[24] Zhang L, Wang CY, Xian HY, Wang J, Zhang YQ, Bao Z, et al. Large magnesium isotopic fractionation in lunar agglutinatic glasses caused by impact-induced chemical diffusion. Geochim Cosmochim Acta 2024;378:71–81.

[25] Sommer C, Straehle C, Köthe U, Hamprecht FA. Ilastik: interactive learning and segmentation toolkit. In: Proceedings of the 2011 IEEE International Symposium on Biomedical Imaging: From Nano to Macro; 2011 Mar 30–Apr 02; Chicago, IL, USA. Piscataway: IEEE; 2011. p. 230–3.

[26] Lasdon LS, Waren AD, Jain A, Ratner M. Design and testing of a generalized reduced gradient code for nonlinear programming. ACM Trans Math Softw 1978;4(1):34–50.

[27] Wang C, Ping W, Bai Q, Cui H, Hensleigh R, Wang R, et al. A general method to synthesize and sinter bulk ceramics in seconds. Science 2020;368(6490):521–6.

[28] Abràmoff MD, Magalhães PJ, Ram SJ. Image processing with ImageJ. Biophoton Int 2004;11(7):36–42.

[29] Lin Z, Zhao X, Wang C, Dong Q, Qian J, Zhang G, et al. Rapid pressureless sintering of glasses. Small 2022;18(17):e2107951.

[30] Warren PH. Lunar rock-rain: diverse silicate impact-vapor condensates in an Apollo-14 regolith breccia. Geochim Cosmochim Acta 2008;72(14):3562–85.

[31] Nemchin AA, Norman MD, Grange ML, Zeigler RA, Whitehouse MJ, Muhling JR, et al. U–Pb isotope systematics and impact ages recorded by a chemically diverse population of glasses from an Apollo 14 lunar soil. Geochim Cosmochim Acta 2022;321:206–43.

[32] Yang W, Chen Y, Wang H, Tian HC, Hui H, Xiao Z, et al. Geochemistry of impact glasses in the Chang'e-5 regolith: constraints on impact melting and the petrogenesis of local basalt. Geochim Cosmochim Acta 2022;335:183–96.

[33] Zellner NEB, Spudis PD, Delano JW, Whittet DCB. Impact glasses from the Apollo 14 landing site and implications for regional geology. J Geophys Res Planets 2002;107(E11):5102.

[34] Elkins-Tanton LT, Chatterjee N, Grove TL. Experimental and petrological constraints on lunar differentiation from the Apollo 15 green picritic glasses. Meteorit Planet Sci 2003;38(4):515–27.

[35] Wentworth SJ, McKay DS, Lindstrom DJ, Basu A, Martinez RR, Bogard DD, et al. Apollo 12 ropy glasses revisited. Meteoritics 1994;29(3):323–33.

[36] Wenk H, Joswig W, Tagai T, Korekawa M, Smith BK. The average structure of $An_{62–66}$ labradorite. Am Mineral 1980;65(1–2):81–95.

[37] Peacor DR. Refinement of the crystal structure of a pyroxene of formula $M_{II}M_{III}(Si_{1.5}Al_{0.5})O_6$. Am Mineral 1967;52(1–2):31–41.

[38] Domeneghetti MC, Tazzoli V, Boffa Ballaran T, Molin GM. Orthopyroxene from the Serra de Magé meteorite: a structure-refinement procedure for a *Pbca* phase coexisting with a *C*2/*c* exsolved phase. Am Mineral 1996;81(7–8):842–6.

[39] Wechsler BA, Prewitt CT. Crystal structure of ilmenite ($FeTiO_3$) at high temperature and at high pressure. Am Mineral 1984;69(1–2):176–85.

[40] Birle J, Gibbs G, Moore P, Smith JV. Crystal structures of natural olivines. Am Mineral 1968;53(5–6):807–24.

[41] Levien L, Prewitt CT, Weidner DJ. Structure and elastic properties of quartz at pressure. Am Mineral 1980;65(9–10):920–30.

[42] Su B, Chen Y, Wang Z, Zhang D, Chen H, Gou S, et al. South Pole-Aitken massive impact 4.25 billion years ago revealed by Chang'e-6 samples. Natl Sci Rev 2025;12(6):nwaf103.

[43] Britt DT, Cannon KM, Donaldson Hanna K, Hogancamp J, Poch O, Beck P, et al. Simulated asteroid materials based on carbonaceous chondrite mineralogies. Meteorit Planet Sci 2019;54(9):2067–82.

[44] Metzger PT, Britt DT, Covey S, Schultz C, Cannon KM, Grossman KD, et al. Measuring the fidelity of asteroid regolith and cobble simulants. Icarus 2019;321:632–46.

[45] Teng Y, Wang S, Cui Y, Pang Y. Influence of loading conditions on mechanical behaviors of lunar regolith simulant WHU-1 based on Chang'e-5 returned samples. Acta Geotech 2025;20(5):2327–44.

[46] Ruan R, Yang W, Zhang D, Tian HC, Zhao Q, Zou Y, et al. A moderate-Ti lunar mare soil simulant: IGG-01. Acta Astronaut 2024;224:148–60.

[47] Xu G, Li Y, Pang R, Chen Z, Ren X. Constitutive model analysis of Chang'e-5 simulated lunar regolith solidified bodies under compression. Case Stud Constr Mater 2024;21:e03704.

[48] Zou Y, Wu H, Chai S, Yang W, Ruan R, Zhao Q. Development and characterization of the PolyU-1 lunar regolith simulant based on Chang'e-5 returned samples. Int J Min Sci Technol 2024;34(9):1317–26.

[49] Wang H, Zhou S, Zhang X, Zhou Q, Jiang Y, Deng Y, et al. Particle morphology controls bulk mechanical behavior of far-side lunar regolith from Chang'e-6 samples and deep Learning. Research 2026;9:1064.

[50] Nie J, Wang S, Cui Y, et al. Analyzing the mechanical heterogeneity of the Chang'e-5 lunar breccia clast: implications for the elastic modulus of lunar rock. J Geophys Res-Planets 2025;130(6):e2024JE008849.

[51] Gualtieri T, Bandyopadhyay A. Compressive deformation of porous lunar regolith. Mater Lett 2015;143:276–8.

[52] Meurisse A, Beltzung JC, Kolbe M, Cowley A, Sperl M. Influence of mineral composition on sintering lunar regolith. J Aerosp Eng 2017;30(4):04017014.

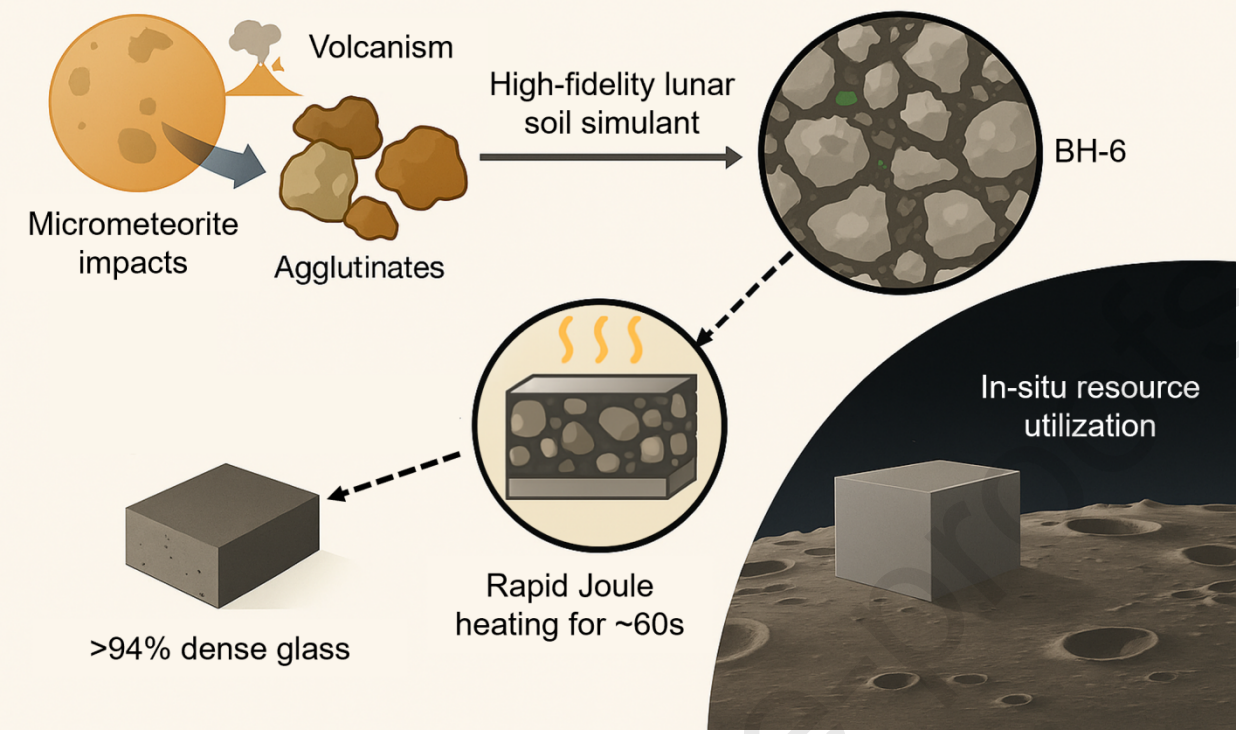
[53] Fateri M, Sottong R, Kolbe M, Gamer J, Sperl M, Cowley A. Thermal properties of processed lunar regolith simulant. Int J Appl Ceram Technol 2019;16(6):2419–28.

[54] Han W, Ding L, Cai L, Zhu J, Luo H, Tang T. Sintering of HUST-1 lunar regolith simulant. Constr Build Mater 2022;324:126655.

[55] Warren P, Raju N, Ebrahimi H, Krsmanovic M, Raghavan S, Kapat J, et al. Effect of sintering temperature on microstructure and mechanical properties of molded martian and lunar regolith. Ceram Int 2022;48(23, Part B):35825–33.

[56] Li J, Thakur A, Li Y, Yang M, Yuxiang G, Linke S, et al. Phase formation and mechanical properties of graphene reinforced regolith composites. Mater Today Commun 2023;35:106112.

[57] Ginés-Palomares JC, Fateri M, Schubert T, de Peindray d'Ambelle L, Simon S, Gluth GJG, et al. Material aspects of sintering of EAC-1A lunar regolith simulant. Sci Rep 2023;13(1):23053.



Declaration of Interest Statement

☒ The authors declare that they have no known competing financial interests or personal relationships that could have appeared to influence the work reported in this paper.

☐ The author is an Editorial Board Member/Editor-in-Chief/Associate Editor/Guest Editor for this journal and was not involved in the editorial review or the decision to publish this article.

☐ The authors declare the following financial interests/personal relationships which may be considered as potential competing interests:

Journal Pre-proofs